



Cite this: DOI: 10.1039/c6nr05809d

## Optofluidic sensing from inkjet-printed droplets: the enormous enhancement by evaporation-induced spontaneous flow on photonic crystal biosilica†

Xianming Kong,<sup>‡a</sup> Yuting Xi,<sup>‡a</sup> Paul LeDuff,<sup>b</sup> Erwen Li,<sup>a</sup> Ye Liu,<sup>a</sup> Li-Jing Cheng,<sup>a</sup> Gregory L. Rorrer,<sup>b</sup> Hua Tan<sup>\*c</sup> and Alan X. Wang<sup>\*a</sup>

Novel transducers for detecting an ultra-small volume of an analyte solution play pivotal roles in many applications such as chemical analysis, environmental protection and biomedical diagnosis. Recent advances in optofluidics offer tremendous opportunities for analyzing miniature amounts of samples with high detection sensitivity. In this work, we demonstrate enormous enhancement factors ( $10^6$ – $10^7$ ) of the detection limit for optofluidic analysis from inkjet-printed droplets by evaporation-induced spontaneous flow on photonic crystal biosilica when compared with conventional surface-enhanced Raman scattering (SERS) sensing using the pipette dispensing technology. Our computational fluid dynamics simulation has shown a strong recirculation flow inside the 100 picoliter droplet during the evaporation process due to the thermal Marangoni effect. The combination of the evaporation-induced spontaneous flow in micron-sized droplets and the highly hydrophilic photonic crystal biosilica is capable of providing a strong convection flow to combat the reverse diffusion force, resulting in a higher concentration of the analyte molecules at the diatom surface. In the meanwhile, high density hot-spots provided by the strongly coupled plasmonic nanoparticles with photonic crystal biosilica under a 1.5  $\mu\text{m}$  laser spot are verified by finite-difference time domain simulation, which is crucial for SERS sensing. Using a drop-on-demand inkjet device to dispense multiple 100 picoliter analyte droplets with pinpoint accuracy, we achieved the single molecule detection of Rhodamine 6G and label-free sensing of  $4.5 \times 10^{-17}$  g trinitrotoluene from only 200 nanoliter solution.

Received 22nd July 2016,  
Accepted 6th September 2016  
DOI: 10.1039/c6nr05809d  
[www.rsc.org/nanoscale](http://www.rsc.org/nanoscale)

### Introduction

The strategy for the rapid and accurate detection of ultra-small volume samples is of great interest for health monitoring, environmental protection, biological experiments, forensics and experiments involving radioactive analytes.<sup>1,2</sup> Recent advances in the fields of photonics and microfluidics have accelerated the development of optofluidics,<sup>3</sup> in which photonic and microfluidic architectures are integrated to synergistically provide an enhanced function and performance, which is

well-suited for biological and chemical detection from a miniature amount of solution. From the photonics perspective, various optical sensing technologies such as refractive index (RI), fluorescence, and surface enhanced Raman scattering (SERS) have been employed in optofluidics to obtain the information of target molecules through their inherent fingerprints.<sup>4–6</sup> For example, SERS spectroscopy can provide vibrational information of a target molecule at a very low concentration even down to single molecule levels.<sup>7–9</sup> The extraordinary sensitivity of SERS primarily relies on the localized surface plasmon resonance (LSPR) effect of the plasmonic substrates.<sup>10–12</sup> When considering fluidic dynamics, microfluidic channels or liquid droplets offer a critical functionality that determines the detection limit through mass transport by performing assays at the microliter to nanoliter volume scale. Unlike continuous flow systems, droplet-based microfluidics can produce and manipulate ultra-small volume aqueous droplets independently with pinpoint accuracy.<sup>13</sup> For example, the inkjet printing technology has become a versatile strategy for biosensing to dispense analytes more efficiently

<sup>a</sup>School of Electrical Engineering and Computer Science, Oregon State University, Corvallis, OR, 97331, USA. E-mail: [wang@eecs.oregonstate.edu](mailto:wang@eecs.oregonstate.edu)

<sup>b</sup>School of Chemical, Biological & Environmental Engineering, Oregon State University, Corvallis, OR, 97331, USA

<sup>c</sup>School of Engineering and Computer Science, Washington State University-Vancouver, Vancouver, WA, 98686, USA. E-mail: [hua.tan@wsu.edu](mailto:hua.tan@wsu.edu)

†Electronic supplementary information (ESI) available. See DOI: 10.1039/c6nr05809d

‡These two authors contributed equally to this manuscript.

with better uniformity compared with conventional pipette dispensing.<sup>14,15</sup>

Recent progress in optofluidic-SERS sensing<sup>5,16</sup> majorly focuses on various approaches to enhance the SERS signals by increasing the binding affinity of analytes to the plasmonic 'hot-spots'. Angelis and coworkers fabricated SERS substrates with super-hydrophobic surfaces and a plasmonic tip, which can concentrate the analyte-containing droplet on the plasmonic tip during the process of evaporation and obtain the SERS signal of Rhodamine 6G (R6G) at the level of a few molecules.<sup>17</sup> Materials with nanoporous structures have also been explored for improving the performance of SERS. Liu *et al.* used a nanoporous polymer monolith within the channel of a microfluidic system for trapping and concentrating silver nanoclusters in a 3-D matrix. This significantly enhanced the SERS intensity and achieved a detection of R6G at 220 fM.<sup>18</sup> Fan's group adopted Au-NP immobilized multi-hole capillaries in optofluidic chips, which can provide 3-D flow-through structures to accommodate more interaction of SERS-active sites with the analytes<sup>16</sup> leading to rapid and sensitive SERS detection.

However, existing research in droplet-based optofluidic sensing including optofluidic-SERS ignored one critical role played by the system—evaporation! Particularly, how droplet evaporation will accelerate the mass transport and hence affect the distribution of analyte molecules on nanostructured optofluidic sensors is not well understood yet. The evaporation of sessile droplets on solid substrates involves a surprisingly complex physico-chemical process. One of the most fascinating effects associated with a drying droplet is the spontaneous evaporation-induced flow that can be generated inside the droplet, which plays an important role in a number of emerging technologies including the self-assembly of nanostructures,<sup>19</sup> printed electronics,<sup>20</sup> biomolecule microarray fabrication,<sup>21</sup> and functional particle coating.<sup>22</sup> The drying of a colloidal droplet often leaves a thin ring-shaped stain along the droplet perimeter (coffee-ring effect) in which most of the solid particles are deposited after evaporation. Deegan *et al.*<sup>23–25</sup> first attributed the coffee-ring effect to the radially outward capillary flow induced by droplet evaporation at a pinned three-phase (liquid–vapor–solid) contact line. However, the droplet evaporation can take a different mode in which the contact line is moving.<sup>26</sup> The underlying causes for the two evaporation modes are not yet understood completely. In addition to the capillary flow, there are other types of spontaneous flows that can be generated within the evaporating droplet because of the temperature-induced or surfactant concentration-induced gradients in surface tension known as Marangoni effects.<sup>27</sup> Hu and Larson<sup>28–30</sup> solved the temperature and fluid flow inside the evaporating droplet and predicted that a significant recirculation flow can develop within the droplet due to the thermal Marangoni effect. Ristenpart *et al.*<sup>31</sup> investigated the effect of the thermal conductivity of the substrate on the thermal Marangoni flow. A number of researchers also employed the surfactant-induced Marangoni flows to counteract the bulk capillary flow to achieve the

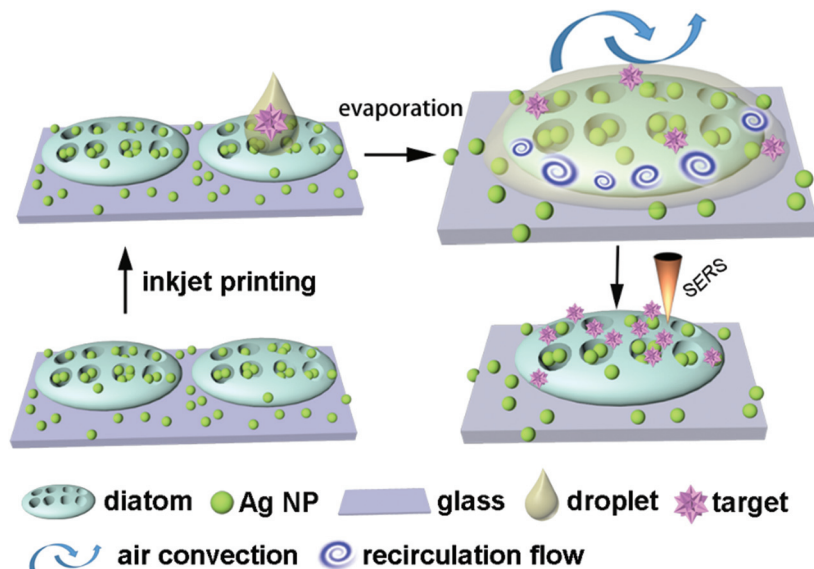
desired deposition patterns of colloidal materials.<sup>32–37</sup> It is noteworthy that the very recent work done by Marin *et al.*<sup>35</sup> for the first time visualized the thermally driven Marangoni flow developed inside the water droplets.

The motivation for this work is to harness the spontaneous evaporation-driven Marangoni flow within the inkjet-printed droplets to significantly accelerate the mass transport of the solvent in biosensors and hence achieve ultra-high sensitivity from ultra-small volume sample solutions using SERS. Particularly in this work, we will focus on diatom-based nanostructured biosensors, which are nature-created photonic crystal biosilica. Diatoms are a type of photosynthetic biomineralized marine organisms with periodic nanopores embedded in the frustules, which enable unique photonic crystal features such as a photonic bandgap,<sup>38</sup> guided mode resonance,<sup>39</sup> and lensless light focusing.<sup>40</sup> Our previous studies have proven that such unique photonic crystal features can enhance the LSPRs of metallic NPs on the surface of diatom frustules, which results in significantly enhanced SERS signals from analytes adsorbed on the metallic NPs.<sup>41,42</sup> In addition, the abundant hydroxyl groups on the surface make diatom photonic crystal biosilica very hydrophilic. However, the function of the hydrophilic surface for biosensing has not been sufficiently explored. In this study, we used a drop-on-demand (DoD) inkjet device to precisely dispense a miniature amount of an analyte into the diatom biosilica through a train of micron-sized droplets. During the droplet evaporation, the combination of a highly hydrophilic surface of diatom frustules can lead to the liquid flow of the droplet from the glass substrate towards the diatom frustules during the evaporation process, *i.e.* the de-pinned contact-line drying and an inward capillary flow. Therefore, the combined effect of the moving contact-line and the Marangoni recirculation flow results in a high concentration of the target molecules on diatom frustules as the illustration in Scheme 1. A numerical study was carried out to gain insight into the evaporation-induced flow of the sessile droplet. During the inkjet deposition of the analyte solution, a time interval of 1 second between two successive firing events allows the drying of the previously landed droplet. As a result, the target molecules in the solution can be quickly and effectively concentrated onto the diatom frustules *via* the evaporation-induced flow of each droplet in a repetitive manner. Our experimental data have shown that the detection sensitivity can be increased by  $10^6$ – $10^7$  times by multiple cycles of dispensing–evaporating processes.

## Results and discussion

### Optical simulation of Ag NPs on photonic crystal biosilica

Although we have simulated a single Ag NP or a dimer Ag NP on photonic crystal biosilica in our previous work,<sup>36</sup> the contribution of the diatom frustule to randomly distributed Ag NPs with high density hot-spots has not been investigated. Such simulation is crucial to understand the mechanism of photonic crystal-enhanced SERS sensing more precisely.<sup>43</sup> We used



**Scheme 1** Illustration of the dispensing of sub-nanoliter liquid droplets to photonic crystal biosilica by inkjet printing. The enormous molecular accumulation effect was achieved by the evaporation-induced spontaneous flow as highlighted by the upper-right figure, which improved the optofluidic SERS sensitivity by  $10^6$ – $10^7$ .

the FullWAVE module of the RSoft photonic component design suite based on the three-dimensional (3-D) finite-difference time-domain (FDTD) algorithm in our study. Fig. 1(a) illustrates the constructed simulation model. The periodic nanopored diatom is modeled as a two-layer structure as shown in the inset figure, and the parameters are derived from our previous SEM characterization:<sup>42</sup> a top layer (120 nm thick) with big air holes (200 nm in diameter) and a bottom layer (60 nm thick) with a small air hole. The period of the diatom structure is 400 nm. Ag NPs of 40 nm diameter are randomly distributed both on the top surface and in the pores of the frustule. The incident light is a 532 nm wavelength Gaussian beam with a beam diameter of 1.5  $\mu\text{m}$ , which matches the laser light spot of our SERS experiment when using a 100 $\times$  objective lens. The boundary condition in the X and Y directions is a perfectly matched layer. Because the SERS enhancement factor (EF) is proportional to the fourth power of the local electrical field amplitude,<sup>44</sup> Fig. 1(b) shows the  $E^4$  enhancement (defined as  $|E/E_0|^4$ ) in the Ag NP layer. The value is averaged along the vertical dimension of the 40 nm Ag NPs to avoid unreasonably high values in the narrowest gap, which is 2 nm in our simulation. It is clearly seen that many of the hot-spots can provide more than  $10^6$  SERS EFs. To quantitatively evaluate the contribution from the photonic crystal structure of diatom biosilica, we constructed the same configuration of Ag NPs except placing them on a flat glass substrate. We obtained a similar optical field distribution using 3-D FDTD and used that to normalize the hot-spots on the diatom frustule. The normalized results of the hot-spots are presented in Fig. 1(c) and we can clearly see that the hot-spots are almost universally enhanced by 10 $\times$ , and some areas may experience more than 100 $\times$  improvement due to the presence of the photonic crystal structure of diatom biosilica. The

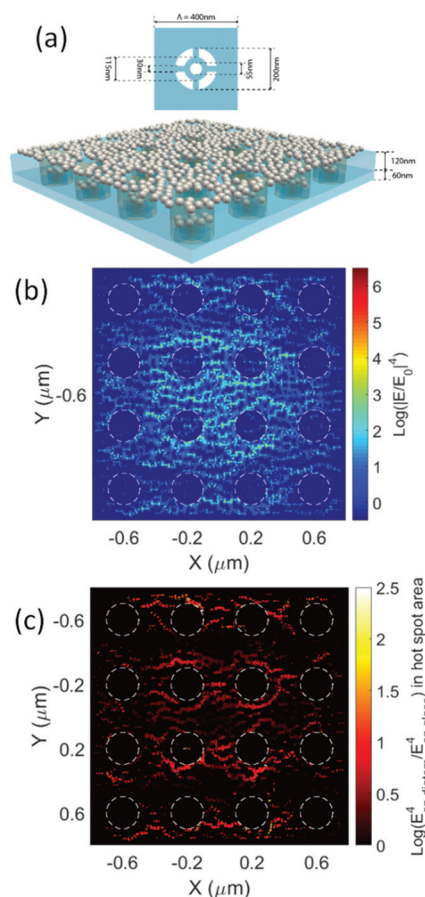


**Fig. 1** (a) Schematic of the 3-D simulated hybrid diatom–Ag NP nanostructures: Ag NPs are randomly distributed on a diatom frustule; (b) 3-D FDTD simulation of the field enhancement  $|E/E_0|^4$  of the nanostructure; and (c) enhancement factor of the hot-spots compared with those of Ag NPs on a flat glass substrate. Note: the value of  $|E/E_0|^4$  is plotted in the log-scale.

optical simulation results roughly match our previous experimental results of 6–12× improvement of the SERS signal intensity.<sup>41,42</sup>

### Microfluidic simulation of the evaporation-induced flow

To gain insight into the evaporation-induced flow for the micrometer-sized droplet, we ran a 2-D simulation of a single inkjet-printed droplet on the diatom frustule. Our focus is the spontaneous flow of the droplet outside the diatom shell during the evaporation, so the diatom is modeled with a curved thin impermeable surface for simplicity. Since the bond between the diatom frustules and the glass substrate is not perfect, we consider a gap of 2 μm between the diatom and glass surface in the simulation to allow liquid flow into and out of the diatom frustule. The ambient temperature is 303 K and the relative humidity is 30%.

The evolution of the evaporating droplet profile predicted from the simulation is shown in Fig. 2(a). The predicted drying time for a droplet of 100 pico-liter (pL) is 1.1 seconds that matches well with the experiment. The contact line in our simulation is moving rather than pinned during evaporation, because the diatom biosilica are more hydrophilic than the glass slide due to the abundant hydroxyl groups on the diatom frustule. The temperature contour at different times is plotted in Fig. 2(b). The temperature in the center of the droplet is around 3 K lower than the contact-line region due to a stronger evaporative cooling effect. Our finding on the direction of the temperature gradient agrees with the asymptotic analysis done by Ristenpart *et al.*<sup>31</sup> The temperature gradient at the droplet-vapor interface results in a gradient in surface tension, as the surface tension decreases with increasing temperature. The non-uniform surface tension induces the motion of the fluid in the direction of the thermal gradient (from the edge to the center), leading to the recirculation in the inner region of the droplet as indicated by the streamline shown in Fig. 2(c). The Marangoni number defined as  $Ma = \sigma_T \rho c_p \Delta T R / \mu k$  is 14.1 (where  $\sigma_T$  derivative of surface-tension to temperature  $\partial\sigma/\partial T = 1.657 \times 10^{-4} \text{ N m}^{-1} \text{ K}^{-1}$ , density  $\rho = 1000 \text{ kg m}^{-3}$ , viscosity  $\mu = 0.001 \text{ kg m}^{-1} \text{ s}^{-1}$ , specific heat  $c_p = 4137.5 \text{ J kg}^{-1} \text{ K}^{-1}$ , conductivity  $k = 0.6 \text{ W m}^{-1} \text{ K}^{-1}$ , drop contact radius

$R = 80 \text{ μm}$ , temperature difference  $\Delta T = 3 \text{ K}$ ), which implies that the thermo-capillary force is more important compared to the viscous force. Fig. 2(d) shows that there is a strong air flow in the vicinity near the liquid–air interface induced by the thermo-capillary liquid flow due to the surface tension gradient. Such air convection can enhance the evaporation rate of the droplet, which is often ignored in previous numerical studies in the literature. As a consequence of the air convection, the average radial velocity of the interface is  $30 \text{ μm s}^{-1}$ , which is much higher than  $1 \text{ μm s}^{-1}$  used in Hu and Larson's study.<sup>29</sup>

The transport of the target molecules to the diatom surface occurs due to both diffusion and convection. From dimensional analysis, we can estimate the time scales for diffusion and convection as  $t_d = R^2/D$  and  $t_c = R/U$ , respectively, where  $R$  is the droplet radius,  $D$  is the molecular diffusivity, and  $U$  is the fluid velocity. Our simulation predicts that the average velocity of the recirculation flow is  $U = 1.2 \times 10^{-4} \text{ m s}^{-1}$ . The diffusivity of the molecules is of the order of  $D = 1 \times 10^{-9} \text{ m}^2 \text{ s}^{-1}$ . So the time scales for diffusion and convection are  $t_d = 11 \text{ s}$  and  $t_c = 0.51 \text{ s}$ , respectively. By comparing the two time scales, we conclude that for micron-sized evaporating droplets, the transport of the molecules is dominated by convection, which is completely different than many optofluidic systems using diffusion-based mass transport.<sup>45,46</sup> Therefore, the thermo-capillary-induced recirculation flow in the droplet during the evaporation process can continuously transport the target molecules to the diatom surface, which greatly increases the local molecule concentration at the surface of Ag NPs that are integrated with diatom frustules. As the intention of this manuscript is only to discover this unique evaporation-driven phenomenon, more rigorous and complete microfluidic simulation is beyond the scope of this paper and will be discussed in the future.

If a large amount of liquid (*e.g.* ~μL) is dispensed into diatom frustules, we expect to see less concentration of target molecules on the diatom surface compared to the case of dispensation of the picoliter-amount liquid. There are two reasons: first, for the large liquid volume, the micrometer-sized diatom frustules will be buried deeply inside the droplet,

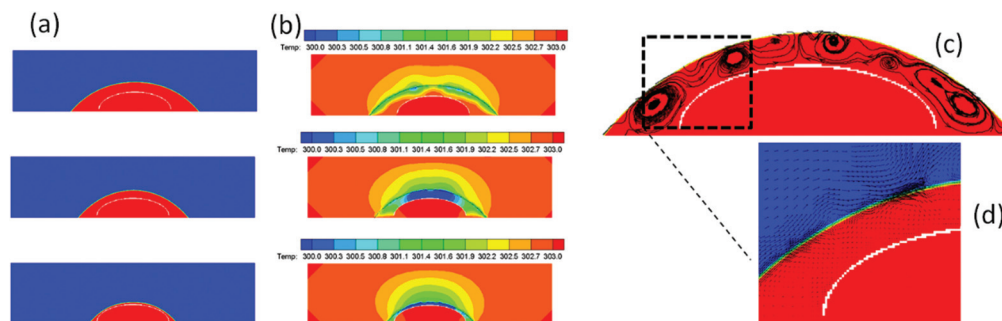


**Fig. 2** (a) The evolution of the droplet profile during the evaporation (the red and the blue represent the liquid and air, respectively; the white curved line represents the diatom shell); (b) the temperature distribution of liquid and air during the evaporation. Recirculation flow due to the thermal Marangoni effect at time = 0.36 s; (c) streamlines within the fluid flow; (d) the close-up of the velocity vector.

so the contact line is likely to be pinned at the glass substrate during evaporation, which results in the concentration of molecules around the droplet perimeter on the glass rather than the diatom surface (conventional coffee-ring effect); second, although the evaporation-induced recirculation flow still exists in the large droplet, the fluid motion is far away from the diatom due to the large volume of the liquid. As a result, the target molecules are more concentrated on the glass rather than the diatom for dispensing a large amount of liquid. Additionally, we expect that using the DoD inkjet device to dispense a large amount of liquid in a repetitive manner (*e.g.* a train of micron-sized droplets) is advantageous over one-time dispensation (*e.g.* conventional pipette dispensing), because the successive evaporation of each individual droplet can cumulatively enhance the concentration of molecules on the diatom surface. As our simulation shows, the diffusion time is much longer than the convection time. Even when the diatom surface has a higher concentration of the molecules than the newly deposited droplet of analyte, the molecules can still be transported to the diatom surface because of the dominating convection effect. Therefore, the strong convection due to the evaporation-induced flow can continuously increase the molecule concentration on the diatom surface through multiple cycles of droplet dispensation and evaporation.

### Optofluidic sensing from inkjet-printed droplets

The integration of the Ag NPs onto the diatom frustules was characterized by scanning electron microscopy (SEM) images as shown in Fig. 3. The morphology and fine structures of diatom (*Pinnularia*) are shown in Fig. 3(a and b). *Pinnularia* is a subcategory of the pennate diatom with a semi-ellipsoidal shape and are nearly 30  $\mu\text{m}$  along the major axis, 7  $\mu\text{m}$  along the minor axis and 5  $\mu\text{m}$  in height. The surface of *Pinnularia* consists of two-dimensional arrays of sub-micron pores with average diameters of 200 nm spaced 400 nm apart from each other (Fig. 3b).

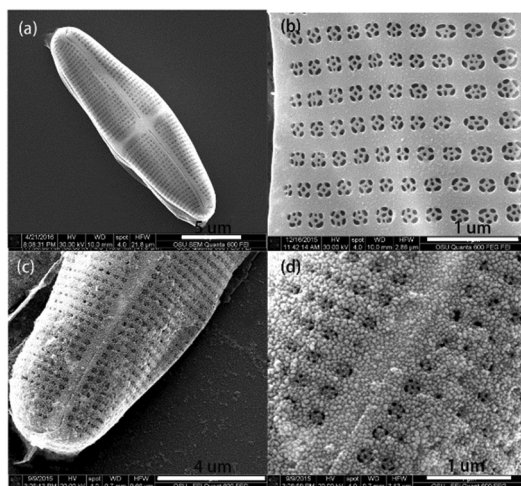


**Fig. 3** SEM images of (a) an overview of a single diatom frustule, (b) arrays of pores on a frustule, (c) and (d) deposited Ag seeds on the diatom frustule *via an in situ* growth method.

The integration of high density Ag NPs on diatom biosilica is difficult by self-assembly techniques due to the repulsion of electrostatic force.<sup>47</sup> The *in situ* growth method was employed to integrate Ag NPs onto diatom biosilica. When the diatom frustule was dipped in an aqueous solution containing mixture of  $\text{SnCl}_2$  and HCl, the  $\text{Sn}^{2+}$  ions could adsorb onto the surface of the diatom due to the affinity with silica. After the diatom was immersed in an aqueous solution of  $\text{AgNO}_3$ , Ag seeds of small diameters were deposited on the entire surface of the diatom through the reaction between  $\text{Sn}^{2+}$  and  $\text{Ag}^+$ . Following the deposition of Ag seeds, large and highly condensed Ag NPs were obtained by immersing the diatom into the growth media (an aqueous mixture of  $\text{AgNO}_3$  and ascorbic acid). The top-view of the diatoms is presented to show the distribution of Ag NPs. It is clearly observed that the Ag NPs immobilized on the diatom were nearly spherical and very uniform, and their diameters are approximately 50 nm (Fig. 3c and d). The microscopy optical image of the diatom frustules and diatom–Ag NPs after ink-printing is shown in Fig. S1.†

We first investigated the sensitivity of the SERS substrate based on diatom biosilica with the *in situ* growth of Ag NPs using a typical SERS-active analyte, R6G, as the probe molecule. One microliter of aqueous R6G solution at  $10^{-6}$  M was drop-cast onto the SERS substrate by a pipette and left to completely dry before SERS measurements. The glass slide with Ag NPs showed no obvious fluorescence interference to the Raman signals (Fig. S2†). Fig. 4a shows the Raman spectra of R6G on the 3-D hybrid plasmonic–biosilica substrate, and a control Raman study on glass–Ag NPs with a similar NP surface density was conducted to evaluate the sensitivity of SERS substrates. Typical SERS spectra of R6G are clearly visible, and the peaks at 1307, 1360, 1506 and  $1650\text{ cm}^{-1}$  are associated with aromatic C–C stretching vibrations of R6G. SERS signals from the 3-D hybrid plasmonic–biosilica substrate are nearly 3 times higher compared with that on the glass–Ag NPs substrate for the Raman peaks of R6G. The additional enhancement of Raman signals is primarily due to the photonic crystal effect of diatom frustules with periodic pores as simulated in Fig. 1, which matches our previous experimental work as well.<sup>41,42</sup>

In order to reduce the sample volume consumption and demonstrate the enhanced sensitivity by evaporation-induced spontaneous liquid flow, the inkjet printing technology was employed for optofluidic SERS sensing. As the liquid sample can be self-driven by the spontaneous flow induced by the evaporation, no pumping system is needed. The volume of one droplet from the inkjet device was around 100 pL. The liquid sample first filled up the tip reservoir of the inkjet printer and was then precisely dispensed to the SERS-active area of the substrate, which is a single diatom at a deterministic location. Compared with the glass substrate, the diatom frustule is highly hydrophilic due to the abundant hydroxyl groups and the nanoporous structure (Fig. S3a†). After being covered by Ag NPs, the surface of diatom frustules is still much more hydrophilic than that of glass–Ag NPs as shown in Fig. S3b.† The hydroxyl groups of diatom biosilica and the glass slide

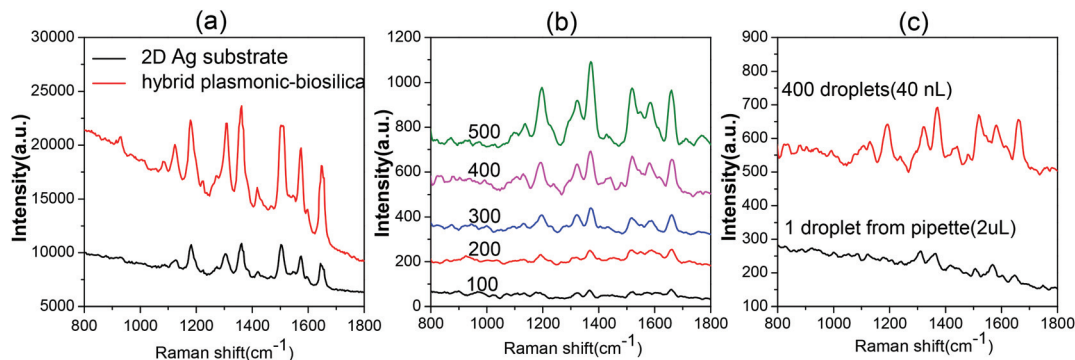


**Fig. 4** (a) Comparison between diatom–Ag NPs and glass–Ag NP SERS substrates: Raman spectra of  $10^{-6}$  M R6G dispensed by a pipette; (b) comparison among the different number of droplets: SERS spectra of R6G (0.1 nM) dispensed onto the diatom–Ag NP substrate by an inkjet printer. (c) Comparison between inkjet printing and pipette dispensing: SERS spectra of R6G (0.1 nM) on the diatom–Ag NP substrates.

were verified by FTIR (Fig. S4†). Therefore, the liquid droplet spread around 120  $\mu\text{m}$  in diameter after impacting the substrate and instantaneously covered the whole diatom frustule because of the hydrophilic biosilica surface, which was visualized by a video from a fluorescence microscope (ESI video†). Right after that, the solution will evaporate within around 1 second.

In general, the intensity of SERS  $I_{\text{SERS}}(V_s)$  can be estimated as:<sup>48,49</sup>

$$I_{\text{SERS}}(V_s) \propto N_M \times |A(V_L)|^2 \times |A(V_s)|^2 \times \delta_{\text{ads}}^R$$

where  $N_M$  is the number of molecules involved in the SERS measurement,  $\delta_{\text{ads}}^R$  is the Raman cross section of the molecule that is being detected, and  $A(V_L)$  and  $A(V_s)$  are the electrical field enhancement factors at the excitation laser and Stokes frequency for the Raman signal enhancement. The other parameters usually are intrinsic factors which are nearly constant for the same SERS substrate and the target molecule.<sup>49</sup> As we mentioned in the previous section, multiple cycles of ‘inkjet printing–evaporation’ processes can accumulate more target molecules, which in turn enhances the SERS signals.

It is very challenging to directly measure the evaporation-induced flow in a micron-sized droplet and the resulting molecule accumulation on the diatom surface in real time. Therefore, we propose to use both SERS and fluorescence imaging to verify the enormous effects produced by inkjet dispensation. Fig. 4(b) shows the SERS spectra of 0.1 nM R6G as a function of the number of ‘inkjet printing–evaporation’ cycles on the diatom with Ag NPs. The observed Raman peaks agree with the stretching modes of R6G. As the number of cycles increased, the SERS signal intensity of R6G was monotonously amplified. These results quantitatively proved that inkjet printing can effectively deliver analyte molecules for optofluidic-SERS sensing. The volume of one droplet from the inkjet device is around 100 pL, thus the total sample consumed in the optofluidic SERS detection is only 100 nL even using 1000 droplets. It is noteworthy that the SERS intensity of 2  $\mu\text{L}$  0.1 nM R6G ( $1.2 \times 10^8$  molecules of R6G) dispensed by a

pipette is even weaker than 40 nL (from 400 droplets) 0.1 nM R6G ( $2.4 \times 10^6$  molecules of R6G) dispensed by the inkjet device as shown in Fig. 4(c). The low analyte delivery efficiency of the pipette comes from two folds. First, the large volume of liquid cast from the pipette led to the spread of the aqueous sample over a larger area, which makes it difficult to achieve a high analyte molecule density under the incident laser spot. Second, the evaporation process of the large droplet ( $\sim 2 \mu\text{L}$ ) on the SERS substrate occurs with a pinned contact line due to the fact that the liquid–gas interface is far away from the hydrophilic diatom surface; therefore, many molecules are transported to the glass substrate rather than the diatom surface with the evaporation-induced flow.

The analyte concentration effect of the diatom was investigated by fluorescence microscopy and spectra. First, 20 nL of R6G ( $10^{-7}$  M) aqueous solution was dispensed onto the glass–diatom substrate *via* 200 droplets by the inkjet printer. The substrate was illuminated by a green laser, as shown in Fig. 5(a). From the optical image, we can observe that there are about 4–5 diatoms that are covered by the inkjet-printed droplets. Therefore, the analyte molecules may accumulate onto multiple diatom frustules. However, the interactions will be minimal as long as the diatom frustules are reasonably far away from each other because the microscopic liquid flow as simulated in Fig. 2 is a local effect. The fluorescence image demonstrated a strong contrast between the diatom and the planar surface of the glass slide. This image confirms that more R6G molecules were transported to the diatom frustule during the process of solution evaporation resulting in a higher analyte concentration on the porous photonic biosilica. This molecule accumulation effect was also confirmed by fluorescence spectra as shown in Fig. 5(b). 2  $\mu\text{L}$  from a pipette and 20 nL from 200 droplets of aqueous solution of R6G at concentrations of  $10^{-6}$  and  $10^{-7}$  M were dispensed to the glass–diatom substrate, respectively. In principle, the amount of R6G molecules contained in 2  $\mu\text{L}$  volume is higher than that in 20 nL volume, but the intensity of the fluorescence spectra was in an opposite manner. The small amount of R6G in 20 nL volume dispensed by inkjet printing shows a higher

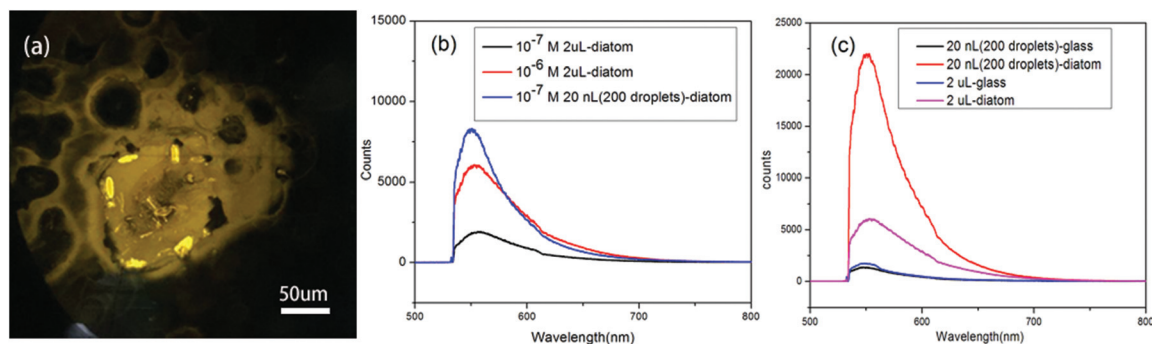


**Fig. 5** (a) Fluorescence image of 200 droplets (20 nL) of aqueous R6G ( $10^{-7}$  M) solution dispensed by the inkjet printer. (b) Fluorescence spectra from diatoms of different amounts of an aqueous solution of R6G dispensed onto the photonic crystal biosilica by inkjet printing and pipette. (c) Comparison of fluorescence spectra of the R6G ( $10^{-6}$  M) dispensed onto the photonic crystal biosilica and the glass substrate by inkjet printing and pipette.

fluorescence intensity than that from 2 μL R6G cast by the pipette. It proves that through multiple cycles of droplet dispensing–evaporation, the analyte concentration effect from the diatom frustule was further enhanced. To quantitatively investigate the molecule accumulation effect compared with the glass substrate, the fluorescence spectra of R6G ( $10^{-6}$  M) on the diatom and glass slides dispensed by inkjet printing and pipette were collected, which are shown in Fig. 5(c). Using inkjet printing, the fluorescence intensity of R6G on diatom frustule is measured to be 17 times higher than that from the glass slide, but the accumulation effect is only 3 times when using the pipette. These results prove that a combination of diatom biosilica with inkjet printed droplets is essential to obtain a large molecular accumulation effect.

In order to quantitatively investigate how multiple cycles of “inkjet printing–evaporation” processes will affect the molecule accumulation, different number of droplets (1, 10, 100 and 1000) of R6G at a concentration of  $10^{-6}$ ,  $10^{-7}$ ,  $10^{-8}$  and  $10^{-9}$  M were dispensed into the diatom SERS substrate, respectively. In principle, the total amount of R6G molecules dispensed onto the SERS substrate is equal to each other, but the intensity of the SERS spectra increases following the increase in the number of droplets as shown in Fig. 6(a). This

abnormal finding suggests that the convection force is much greater than the diffusion force. It can continue to accumulate more and more molecules onto the diatom frustules even after 1000 droplets. It also implies that a single cycle of evaporation cannot sufficiently transport most of the molecules to the diatom frustules because the evaporation lasts only 1 second. However, the successive droplets will dissolve molecules on the glass substrate from previous droplets and continue to transport them onto the diatom frustule. As a comparison, the planar glass slide shows a much smaller accumulation effect for the SERS intensity as in Fig. 6(b). In order to quantitatively compare the molecule accumulation effect, we plotted the most prominent Raman peak of R6G at  $1360\text{ cm}^{-1}$  with respect to different cycles of droplets as shown in Fig. 6(c). For equal amounts of R6G molecules used for inkjet printing, as the number of cycles increases (of course the solution must be diluted accordingly), the enhancement factor from photonic crystal biosilica compared with the glass substrate becomes more and more prominent. The enhancement factor from the glass substrate is measurable only from 1–100 droplets, yet it is still lower than that of photonic crystal biosilica. We attribute this phenomenon to the ‘coffee-ring’ effect of the liquid droplet. However, the molecule accumulation due to the ‘coffee-ring’

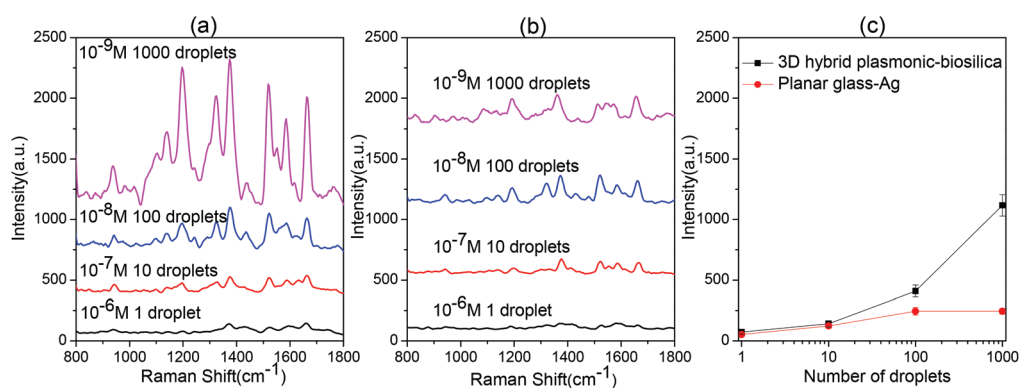


**Fig. 6** Comparison of the number of droplets to dispense the same amount of R6G molecules: SERS spectra of R6G on (a) the diatom–Ag NP substrate and (b) glass–Ag NP substrate by inkjet printing using different combinations of concentration-droplet numbers. (c) SERS signal of the same amount of R6G at  $1360\text{ cm}^{-1}$  with 1, 10, 100 and 1000 droplets dispensed by an inkjet printer.

effect soon saturates when the droplet number is greater than 100. This implies that the convection force induced by the liquid flow on glass is balanced by the diffusion force of the molecules due to the gradient of concentration. Interestingly, there have been some different approaches to concentrate analyte molecules by reducing the initial contact area. Angelis *et al.*<sup>17</sup> used a super-hydrophobic surface to concentrate the analyte into an ultra-small point on the SERS sensing surface after evaporation. However, fabricating such a super-hydrophobic surface requires difficult and complicated processes. In case of a regular glass substrate with a moderate hydrophobic surface, the analyte molecular distribution will not converge to a point. The contact line between the liquid and solid phase is often moving during the drying of the droplet, therefore the molecules/particles tend to evenly spread in the footprint of the initial contact area, instead of concentrating to a small point. Therefore, using hydrophilic nanoporous diatom frustules on regular glass substrates provides an easy-to-implement method to concentrate analytes from inkjet-printed droplets.

To evaluate the enormous enhancement factor by the evaporation-induced spontaneous flow on photonic crystal biosilica, we inkjet printed 2000 droplets of  $10^{-16}$  M R6G solution (only 12 molecules) onto the diatom SERS substrate. In principle, there will be no more than one R6G molecule in the laser spot. Fig. 7(a) shows the detected R6G corresponding to the single molecule signal, the statistic results show that the

detection probability is 30% on the diatom. To demonstrate their application for ultra-sensitive detection from an ultra-small volume sample, we applied this optofluidic SERS technology to detect trinitrotoluene (TNT), which is one of the most common constituents in explosives. Although the SERS method has achieved an ultra-high detection sensitivity for TNT sensing, most of the techniques require surface functionalization of the SERS substrates and the Raman signals actually originate from the probe molecules rather than TNT<sup>50,51</sup> because of the low affinity between TNT and plasmonic NPs. No label-free SERS methods with good sensitivity through the direct detection of TNT signature peaks have been reported. Fig. 7(b) shows the SERS spectra of 2000 droplets of TNT at different concentrations by inkjet printing on the photonic crystal biosilica. The peak located at  $1342\text{ cm}^{-1}$  is assigned to the stretching modes of the  $\text{NO}_2$  group of TNT. The minimum detectable TNT concentration in aqueous solution is below 1 pM, while the detection limit is  $1\text{ }\mu\text{M}$  using a conventional pipette. Therefore, we conclude an enormous enhancement factor of  $10^6$  by the evaporation-induced spontaneous flow on photonic crystal biosilica. More interestingly, the total consumed volume of the solution was only 200 nL, corresponding to  $4.5 \times 10^{-17}$  grams of TNT. If we compare the enhancement factor of the detection limit in terms of the amount of TNT molecules, the enhancement factor is  $10^7$ ! The SERS mapping image of TNT could further visualize the enhancement factor from diatom biosilica (S5†).

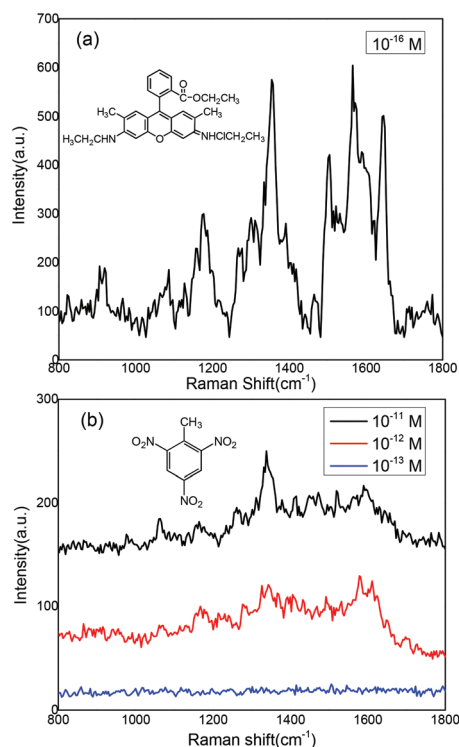


**Fig. 7** Ultra-sensitive optofluidic-SERS detection on the diatom–Ag NP platform by an inkjet printer: (a) SERS spectra of 2000 droplets of R6G ( $10^{-16}$  M); and (b) SERS spectra of 2000 droplets of TNT with different concentrations.

## Conclusions

In conclusion, this study reveals a new optofluidic mechanism for SERS sensing based on the evaporation-induced spontaneous flow on hydrophilic photonic crystal biosilica, which has been qualitatively predicted by our fluid dynamic simulation and quantitatively verified by our experimental results using inkjet printed liquid droplets. Different than most optofluidic sensors relying on slow diffusion-based mass transport, the strong convection flow induced by the liquid droplet evaporation in our optofluidic-SERS substrate not only accelerates the mass transport rate, but also provides a reverse force against the diffusion process, resulting in significant accumulation of the analyte molecules at the diatom surface. When combined with the photonic crystal-enhanced plasmonic hot-spots, we were able to achieve  $10^6$ – $10^7$  enormous enhancement factors in the detection limit. Our experimental results obtained the single molecule detection of R6G and label-free sensing of  $4.5 \times 10^{-17}$  g TNT from only 200 nL liquid samples.

## Experimental

### Materials and reagents

Silver nitrate ( $\text{AgNO}_3$ ) was purchased from Alfa Aesar. Ethylene-diaminetetraacetic acid (EDTA), tin(II) chloride ( $\text{SnCl}_2$ ) and ascorbic acid were obtained from Sigma-Aldrich.

Trisodium citrate ( $\text{Na}_3\text{C}_6\text{H}_5\text{O}_7$ ), hydrochloric acid (HCl), sodium hydroxide (NaOH), ethanol and acetone were purchased from Macron. Rhodamine 6G (R6G) was obtained from TCI. The chemical reagents used were of analytical grade. Water used in all experiments was deionized and further purified by using a Millipore Synergy UV Unit to a resistivity of  $\sim 18.2 \text{ M}\Omega \text{ cm}$ .

### Instruments and measurement

Scanning electron microscopy (SEM) images were acquired on an FEI Quanta 600 FEG SEM with a 15–30 kV accelerating voltage. Printing experiments were carried out using a single-jet stationary thermal inkjet print-head Microjet (HP Inc., OR, USA). The printing processes were controlled using the software from HP, and the volume of the droplet and interval time between droplets could be controlled during the process of printing. The droplet volume was 100  $\mu\text{L}$ . The interval time between two droplets was 1.1 seconds to allow evaporation of the dispensed droplets. The Raman spectra were collected under ambient conditions using a Horiba Jobin Yvon Lab Ram HR800 Raman microscope equipped with a CCD detector, and a 50 $\times$  objective lens was used for the spectral measurement. The excitation wavelength was 532 nm with a laser spot size of 1.5  $\mu\text{m}$  in diameter. The confocal pinhole was set to a diameter of 200  $\mu\text{m}$ . Raman mapping images were acquired with a 100 $\times$  objective lens with a 20  $\times$  20 point mapping array. They were collected under the DuoScan module, with a 0.5 s accumulation time, and collected in the Raman spectral range from 800  $\text{cm}^{-1}$  to 1800  $\text{cm}^{-1}$ . Each spectrum was based on the average of 25 recorded spectra: we chose different diatoms, and recorded the SERS spectra from five different spots on each diatom. Spectra were recorded and processed with Horiba LabSpec software. Fluorescence spectra were acquired according to the method proposed by Aroca's group.<sup>52</sup> Briefly, we point to a diatom surface with the 50 $\times$  objective lens, with the Horiba Jobin Yvon Lab Ram HR800 Raman system using the 532 nm laser line. Fluorescence microscopy images were obtained using the Olympus IX73 microscope equipped with an X-cite 120 LED fluorescence microscope light source.

### Preparation of diatom biosilica with the photonic crystal feature

Diatom cells (*Pinnularia* sp.) were cultivated according to the method previously described with little modification.<sup>53</sup> In this study, diatoms were cultured in 500 mL flasks for 7 days, and diatom suspensions were centrifuged and dispersed with 40 ml of sterile filtered artificial seawater. The suspended diatom cells were transferred into new centrifuge tubes after filtering with a 20  $\mu\text{m}$  mesh sieve, the cell density was diluted to  $2.5 \times 10^5$  cells per ml for seeding. The glass coverslip was set into an individual Petri dish separately, and 15 ml of the diatom cell suspension was transferred into the substrate. The substrates were incubated in a humidifier chamber for an hour to allow cells to settle on the surface, the glass coverslip was transferred from the old Petri dish to a new one. The samples were kept in the humidifier for one day and immersed

in EtOH (70%) for 4 h, and then immersed in pure EtOH for 4 more h. The samples were dried in air and cleaned in a UV ozone cleaner at 90  $^\circ\text{C}$  for 24 h. After that, the glass–diatom substrates were ready for future use after cooling down.

### *In situ* synthesis of silver nanoparticles on diatom biosilica

The procedure for the *in situ* decoration of the highly dense Ag nanoparticles on diatom biosilica was according Chang's method with a little modification.<sup>54</sup> The porous diatom biosilica was immersed in an aqueous solution containing a mixture of  $\text{SnCl}_2$  (20 mM) and HCl (20 mM) for 5 min depositing  $\text{Sn}^{2+}$  on the pore walls. The diatoms were rinsed with water and subsequently washed with acetone and dried under a hydrogen flow. Then the diatoms were immersed in a 20 mM aqueous solution of  $\text{AgNO}_3$  for 2 min to decorate the silver seeds of small sizes on the surface followed by a washing step. The decoration of silver nanoparticle seeds was repeated three times to provide a high density of particle distribution. Then the diatoms were immersed in aqueous solution with 1 mL of 5 mM  $\text{AgNO}_3$  and 0.5 mL of 50 mM ascorbic acid, the Ag seeds grew to Ag NPs of a bigger diameter. After 5 minutes the diatoms were rinsed thoroughly with Milli-Q water and kept in water for further application.

## Acknowledgements

The authors would like to acknowledge the support from the National Institutes of Health under Grant No. 1R03EB018893 and 9R42ES024023. This work was also supported by the U.S. Department of Defense, Office of Naval Research, Synthetic Biology Program, award number N000141210313.

## References

- 1 S. Groh, P. Diwakar, C. Garcia, A. Murtazin, D. Hahn and K. Niemax, *Anal. Chem.*, 2010, **82**, 2568–2573.
- 2 F. Piraino, F. Volpetti, C. Watson and S. J. Maerkl, *ACS Nano*, 2016, 1699–1710.
- 3 X. Fan and I. M. White, *Nat. Photonics*, 2011, **5**, 591–597.
- 4 S. H. Yazdi and I. M. White, *Anal. Chem.*, 2012, **84**, 7992–7998.
- 5 X. Zhao, J. Xue, Z. Mu, Y. Huang, M. Lu and Z. Gu, *Biosens. Bioelectron.*, 2015, **72**, 268–274.
- 6 H. Zhu and X. Fan, *Biosens. Mol. Technol. Cancer Diagn.*, 2012, 125.
- 7 S. Nie and S. R. Emory, *Science*, 1997, **275**, 1102–1106.
- 8 K. Kneipp, Y. Wang, H. Kneipp, L. T. Perelman, I. Itzkan, R. R. Dasari and M. S. Feld, *Phys. Rev. Lett.*, 1997, **78**, 1667.
- 9 H. Xu, E. J. Bjerneld, M. Käll and L. Börjesson, *Phys. Rev. Lett.*, 1999, **83**, 4357.
- 10 K. A. Willets, *Chem. Soc. Rev.*, 2014, **43**, 3854–3864.
- 11 X. Xu, K. Kim, H. Li and D. Fan, *Adv. Mater.*, 2012, **24**, 5457–5463.

- 12 Y. Fang, H. Wei, F. Hao, P. Nordlander and H. Xu, *Nano Lett.*, 2009, **9**, 2049–2053.
- 13 O. J. Miller, A. El Harrak, T. Mangeat, J.-C. Baret, L. Frenz, B. El Debs, E. Mayot, M. L. Samuels, E. K. Rooney and P. Dieu, *Proc. Natl. Acad. Sci. U. S. A.*, 2012, **109**, 378–383.
- 14 D. L. Baluya, T. J. Garrett and R. A. Yost, *Anal. Chem.*, 2007, **79**, 6862–6867.
- 15 B. Derby, *J. Mater. Chem.*, 2008, **18**, 5717–5721.
- 16 Y. Guo, M. K. Khaing Oo, K. Reddy and X. Fan, *ACS Nano*, 2011, **6**, 381–388.
- 17 F. De Angelis, F. Gentile, F. Mecarini, G. Das, M. Moretti, P. Candeloro, M. Coluccio, G. Cojoc, A. Accardo and C. Liberale, *Nat. Photonics*, 2011, **5**, 682–687.
- 18 J. Liu, I. White and D. L. DeVoe, *Anal. Chem.*, 2011, **83**, 2119–2124.
- 19 V. Vohra, A. Bolognesi, G. Calzaferri and C. Botta, *Langmuir*, 2010, **26**, 1590–1593.
- 20 A. Shimoni, S. Azoubel and S. Magdassi, *Nanoscale*, 2014, **6**.
- 21 J. M. Moran-Mirabal, C. P. Tan, R. N. Orth, E. O. Williams, H. G. Craighead and D. M. Lin, *Anal. Chem.*, 2007, **79**, 1109–1114.
- 22 M. Layani, M. Gruchko, O. Milo, I. Balberg, D. Azulay and S. Magdassi, *ACS Nano*, 2009, **3**, 3537–3542.
- 23 R. D. Deegan, O. Bakajin, T. F. Dupont, G. Huber, S. R. Nagel and T. A. Witten, *Nature*, 1997, **389**, 827–829.
- 24 R. D. Deegan, *Phys. Rev. E*, 2000, **61**, 475–485.
- 25 R. D. Deegan, O. Bakajin, T. F. Dupont, G. Huber, S. R. Nagel and T. A. Witten, *Phys. Rev. E*, 2000, **62**, 756–765.
- 26 R. G. Picknett and R. Bexon, *J. Colloid Interface Sci.*, 1977, **61**, 336–350.
- 27 L. E. Scriven and C. V. Sternling, *Nature*, 1960, **187**, 186–188.
- 28 H. Hu and R. G. Larson, *J. Phys. Chem. B*, 2002, **106**, 1334–1344.
- 29 H. Hu and R. G. Larson, *Langmuir*, 2005, **21**, 3972–3980.
- 30 H. Hu and R. G. Larson, *J. Phys. Chem. B*, 2006, **110**, 7090–7094.
- 31 W. D. Ristenpart, P. G. Kim, C. Domingues, J. Wan and H. A. Stone, *Phys. Rev. Lett.*, 2007, **99**, 234502.
- 32 W. Sempels, R. De Dier, H. Mizuno, J. Hofkens and J. Vermant, *Nat. Commun.*, 2013, **4**, 1757.
- 33 T. Still, P. J. Yunker and A. G. Yodh, *Langmuir*, 2012, **28**, 4984–4988.
- 34 J. Park and J. Moon, *Langmuir*, 2006, **22**, 3506–3513.
- 35 A. Marin, R. Liepelt, M. Rossi and C. J. Kahler, *Soft Matter*, 2016, **12**, 1593–1600.
- 36 R. Dou and B. Derby, *Langmuir*, 2012, **28**, 5331–5338.
- 37 M. Pack, H. Hu, D.-O. Kim, X. Yang and Y. Sun, *Langmuir*, 2015, **31**, 7953–7961.
- 38 T. Fuhrmann, S. Landwehr, M. El Rharbi-Kucki and M. Sumper, *Appl. Phys. B*, 2004, **78**, 257–260.
- 39 J. Noyes, M. Sumper and P. Vukusic, *J. Mater. Res.*, 2008, **23**, 3229–3235.
- 40 L. De Stefano, I. Rea, I. Rendina, M. De Stefano and L. Moretti, *Opt. Express*, 2007, **15**, 18082–18088.
- 41 F. Ren, J. Campbell, X. Wang, G. L. Rorrer and A. X. Wang, *Opt. Express*, 2013, **21**, 15308–15313.
- 42 F. Ren, J. Campbell, G. L. Rorrer and A. X. Wang, *IEEE J. Sel. Top. Quantum Electron.*, 2014, **20**, 127–132.
- 43 Z. Mu, X. Zhao, Y. Huang, M. Lu and Z. Gu, *Small*, 2015, **11**, 6036–6043.
- 44 C. M. Aikens, L. R. Madison and G. C. Schatz, *Nat. Photonics*, 2013, **7**, 508–510.
- 45 R. Hansen, H. Bruus, T. H. Callisen and O. Hassager, *Langmuir*, 2012, **28**, 7557–7563.
- 46 T. M. Squires, R. J. Messinger and S. R. Manalis, *Nat. Biotechnol.*, 2008, **26**, 417–426.
- 47 M. R. Ivanov, H. R. Bednar and A. J. Haes, *ACS Nano*, 2009, **3**, 386–394.
- 48 C. V. Raman and K. S. Krishnan, *Nature*, 1928, **121**, 501–502.
- 49 D. Choi, T. Kang, H. Cho, Y. Choi and L. P. Lee, *Lab Chip*, 2009, **9**, 239–243.
- 50 K. A. Mahmoud and M. Zourob, *Analyst*, 2013, **138**, 2712–2719.
- 51 X. He, H. Wang, Z. Li, D. Chen, J. Liu and Q. Zhang, *Nanoscale*, 2015, **7**, 8619–8626.
- 52 A. R. Guerrero and R. F. Aroca, *Angew. Chem., Int. Ed.*, 2011, **50**, 665–668.
- 53 C. Jeffryes, T. Gutu, J. Jiao and G. L. Rorrer, *ACS Nano*, 2008, **2**, 2103–2112.
- 54 S. Chang, Z. A. Combs, M. K. Gupta, R. Davis and V. V. Tsukruk, *ACS Appl. Mater. Interfaces*, 2010, **2**, 3333–3339.